Lipidome profiling with Raman microspectroscopy identifies macrophage response to surface topographies of implant materials

Nora Feuerer[a,b], Julia Marzi[a,b,c], Eva M. Brauchle[a,b,c], Daniel A. Carvajal Berrio[b,c], Florian Billing[a], Martin Weiss[a,d], Meike Jakobi[a], Nicole Schneiderhan-Marra[a], Christopher Shipp[a], and Katja Schenke-Layland[a,b,c,e,1]

[a]NMI Natural and Medical Sciences Institute at the University of Tübingen, 72770 Reutlingen, Germany; [b]Institute of Biomedical Engineering, Department for Medical Technologies and Regenerative Medicine, Eberhard Karls University Tübingen, 72076 Tübingen, Germany; [c]Cluster of Excellence "Image-Guided and Functionally Instructed Tumor Therapies", Eberhard Karls University Tübingen, 72076 Tübingen, Germany; [d]Department of Women's Health, Research Institute for Women's Health, Eberhard Karls University Tübingen, 72076 Tübingen, Germany; and [e]Department of Medicine, Division of Cardiovascular Medicine, University of California, Los Angeles, CA 90095

Edited by Cato Laurencin, UConn Health, Farmington, CT; received July 25, 2021; accepted November 16, 2021

Biomaterial characteristics such as surface topographies have been shown to modulate macrophage phenotypes. The standard methodologies to measure macrophage response to biomaterials are marker-based and invasive. Raman microspectroscopy (RM) is a marker-independent, noninvasive technology that allows the analysis of living cells without the need for staining or processing. In the present study, we analyzed human monocyte-derived macrophages (MDMs) using RM, revealing that macrophage activation by lipopolysaccharides (LPS), interferons (IFN), or cytokines can be identified by lipid composition, which significantly differs in M0 (resting), M1 (IFN-γ/LPS), M2a (IL-4/IL-13), and M2c (IL-10) MDMs. To identify the impact of a biomaterial on MDM phenotype and polarization, we cultured macrophages on titanium disks with varying surface topographies and analyzed the adherent MDMs with RM. We detected surface topography–induced changes in MDM biochemistry and lipid composition that were not shown by less sensitive standard methods such as cytokine expression or surface antigen analysis. Our data suggest that RM may enable a more precise classification of macrophage activation and biomaterial–macrophage interaction.

macrophage polarization | Raman imaging | innate immunity | biomaterials | Raman spectroscopy

Macrophages play an essential role in our innate immune system. They patrol tissues, detect pathogens, and respond to tissue damage (1–3). Macrophages remove pathogens and cellular debris through phagocytosis and encapsulation, and they control downstream processes such as wound healing and tissue regeneration (4, 5). To accommodate the multitude of tasks, macrophages exhibit a high degree of plasticity, which allows them to reversibly adopt different phenotypes within a short period of time (6–8). Macrophage activation is dependent on a variety of bioactive molecules and is usually controlled by complex signaling pathways in vivo. Macrophages are typically classified into the following categories: M0 (resting), M1 (proinflammatory), and M2 (anti-inflammatory). M2 macrophages are further divided into fibrotic (M2a) and regenerative (M2c) subtypes (9). This classification is not definite, as many other activation states exist (10).

Adverse immune reactions toward implant materials are known to cause chronic inflammation, tissue loss, aseptic loosening, and fibrotic encapsulation (11, 12). This process is typically associated with significant pain for the patient, the need for repeated surgeries, and implant replacement (13, 14). Recently, materials designed to modulate the immune response have seen intense interest, as they may improve implant durability and integration (15). Macrophages are key cells in this process and are highly sensitive to material surface characteristics such as topography, stiffness, or wettability (16–21). However, how these properties impact macrophage behavior is not fully understood.

Macrophage classification is typically performed using techniques such as flow cytometry (FC), analyzing RNA expression, or enzyme-linked immunosorbent assays. These end-point analytical techniques require complex processing and invasive reagents such as antibodies and primers. Cells are not analyzed in their native state, and the focus is on the expression of only predefined marker genes or proteins. As macrophage polarization is in flux, their classification into discrete categories based on a priori defined markers can be problematic (22).

Raman microspectroscopy (RM) has emerged as a powerful tool for the investigation of living cells, assessing their physiology and biochemical composition on a single-cell level without the need for processing or staining (23). RM can be used to identify chemical fingerprints or patterns of distinct cellular components such as nucleic acids, proteins, and lipids (24, 25). Previous research has demonstrated that RM can be used to reliably distinguish between different cell phenotypes or stages of the cell cycle based on the spectral information obtained by RM (25–29).

In this study, we present an approach for in situ macrophage characterization and monitoring their response to distinct surface

Significance

Macrophage plasticity and activation dynamics are under intense investigation because their full complexity cannot be captured by the few predefined markers that are commonly used. Macrophages are highly adherent and respond to surface microstructures in a sensitive manner. Here, we use Raman microspectroscopy and Raman imaging to study the macrophage response to defined activation stimuli and transfer these findings to macrophages cultured on titanium with varying surface roughness. We show that Raman-based methods can discriminate between macrophage phenotypes noninvasively and without the need to use antibody-based cell markers.

Author contributions: N.F., J.M., E.M.B., C.S., and K.S.-L. designed research; N.F., J.M., D.A.C.B., and M.J. performed research; M.W. contributed new reagents/analytic tools; N.F., J.M., D.A.C.B., F.B., M.J., and K.S.-L. analyzed data; M.W. ensured accordance of the study with ethical guidelines; and N.F., J.M., E.M.B., F.B., N.S.-M., and K.S.-L. wrote the paper.

The authors declare no competing interest.

This article is a PNAS Direct Submission.

[1]To whom correspondence may be addressed. Email: katja.schenke-layland@uni-tuebingen.de.

This article contains supporting information online at http://www.pnas.org/lookup/suppl/doi:10.1073/pnas.2113694118/-/DCSupplemental.

Published December 21, 2021.

features of titanium. By analyzing Raman spectral fingerprints of activated macrophages, we were able to characterize the cell response without detaching or exogenously labeling the cells. Information derived from these data provides valuable insight into macrophage physiology on a level that is not achievable by classical analytical techniques, potentially providing information for the field of macrophage activation. Furthermore, we demonstrate that RM can analyze material-adherent cells and that the resulting spectral information can be used to classify the macrophage response into the existing activation spectrum.

Results

We characterized lipid spectra of four distinctively polarized human monocyte-derived macrophage (MDM) subtypes: M0 (resting), M1 (lipopolysaccharides [LPS]/IFN-γ), M2a (IL-4/IL-13), and M2c (IL-10) by RM. We provide evidence that Raman lipid fingerprint spectra can be used to assess activation states of adherent macrophages without additional treatment, providing insights into the impact of biomaterial surface characteristics like topography and roughness.

Establishment of a Human Macrophage in vitro Model for RM. A human macrophage in vitro polarization model was validated by thoroughly assessing the immune response of MDMs isolated from six healthy individual donors (three female and three male) toward polarization stimuli. Morphological characteristics, surface marker expression, and cytokine secretion are outlined in Fig. 1. Distinct morphological features such as the "fried egg" morphology (Fig. 1 *A* and *B*), spindle-shaped elongation (Fig. 1 *C* and *D*), or a mixture of both (Fig. 1*A*) are observable by light microscopy (Fig. 1 *A–D*). Surface marker expression measured by FC of CD86 and human leukocyte antigen–DR isotype (HLA-DR) was significantly enhanced in M1 and M2a macrophages but not in M2c (Fig. 1 *E* and *F*). In contrast, M2a macrophages exhibited a significantly increased CD206 expression compared with M0 and M1 (Fig. 1*G*), while the same could be observed for M2c macrophages regarding CD163 (Fig. 1*H*). These findings were confirmed by imaging FC and microscopy images, of which we assessed mean fluorescence intensities (MFIs in Fig. 1*I*).

Cytokine secretion was analyzed by Luminex technology to further characterize the immunological response toward polarization stimuli (Fig. 1 *J–Q*). A significant increase in proinflammatory cytokines secreted by M1 macrophages, such as IL-6, TNF-α, IL-8, and IL-1β, was observed, while MIP-1β and IL-1RA were increased in M2a macrophages and MCP-1 was increased in M2c macrophages.

Raman Imaging Resolves Subcellular Structures in MDMs. MDMs from the same donors were polarized, detached, fixed, and analyzed by RM. Raman imaging was employed to resolve subcellular structures of macrophages and to better visualize changes between polarization states. Using true component analysis (TCA), three main cellular components were identified that could be attributed to nucleic acids, proteins, and lipids based on their location within the cell (Fig. 2 *A–D*) and their Raman fingerprint spectra (Fig. 2*E*). By comparing the average lipid spectrum to reports in the literature, triacylglycerides (TAGs) were identified as the main constituent of the lipid component (30). This was confirmed by in-house measurements of reference spectra. For comparison, a typical TAG spectrum is shown in Fig. 2*E* (TAG and glyceryl trioleate).

Raman Lipid Spectra Identify Spectral Differences between Polarized MDMs. To determine if RM can differentiate between different macrophage polarization states, Raman spectra of each component were extracted and an average spectrum per cell and component was calculated. Average spectra for each subcellular structure were analyzed by principal component analysis (PCA) identifying that the best separation of all subtypes was achieved by the lipid component as shown in *SI Appendix*, Fig. 1 *A–C*.

The lipid component of each cell was extracted, and 2% of the most intense component spectra were analyzed by PCA revealing distinct score clusters of M1 and M2a macrophages (Fig. 3*A*). Statistical analysis of the PC score values confirmed significant separation between all four subtypes (Fig. 3 *B* and *C*). To identify Raman peaks responsible for the separation, PC loadings were plotted, and prominent peaks were identified as indicated by the black arrows (Fig. 3 *D* and *E*). Particularly pronounced were peaks in the lipid region at 1,655 cm^{-1}, 2,855 cm^{-1}, 2,965 cm^{-1}, and 2,980 cm^{-1}. All relevant peaks and their molecular assignments are listed in *SI Appendix*, Table 1.

For a more in-depth understanding of the molecular composition of the lipid component, an average spectrum for each MDM subtype was extracted (Fig. 3*F*, M0 through M2c) and compared to typical lipid spectra from the literature, indicating linoleic and palmitoleic acid as likely constituents (30). Reoccurring prominent peaks in the loading plots as well as the average spectra were located at Raman shifts of 1,440 cm^{-1}, 1,655 cm^{-1}, 2,855 cm^{-1}, 2,935 cm^{-1}, and 3,010 cm^{-1}.

To assess if the impact of substrate topography on macrophage phenotype can be analyzed in situ on a single-cell basis, we tested monocyte polarity on different surfaces. Human monocytes from three of the previous donors were seeded and cultured on glass (control) and two types of titanium disks with distinct surface topographies: 1) machine-polished titanium (Ti M) with a smooth surface pattern of parallel grooves and 2) acid-etched titanium (Ti A) with a rough surface (Fig. 4 *A–C*). Regions of interest (ROIs) of 150 × 150 μm were scanned, and Raman spectra were analyzed by TCA (Fig. 4 *D–F*). All three major cellular components were identified by TCA in MDMs cultured on glass, Ti M and Ti A. For validation purposes, MDM response toward the different substrates was also evaluated by classical antigen expression and cytokine secretion. We identified that the physiological response of MDMs cultured on biomaterial substrates was less pronounced compared to actively polarized MDMs. All surface antigens remained at resting level except CD206, which was significantly increased in MDMs cultured on Ti A (Fig. 4 *G–J*). The tested substrates did not trigger a release of proinflammatory cytokines such as TNF-α or IL-8 (Fig. 4 *K* and *L*). Notably, MIP-1β was not secreted in substrate-adherend MDMs, despite being highly expressed in both M1 and M2a macrophages (Fig. 4*M*). Instead, a moderate increase in MCP-1 was observed in MDMs cultured on Ti A, a cytokine that was also increased in M2c macrophages (Fig. 4*N*).

Average lipid RM spectra of substrate-activated MDMs were analyzed by PCA in order to assess if previously generated Raman lipid fingerprints could be employed to classify MDMs of an unknown activation state (Fig. 5*A*). Loading plots showed a separation based on the same bands as observed in the targeted polarization experiment in Fig. 3. PC loadings revealed major peaks at 1,005 cm^{-1}, 1,340 cm^{-1}, 1,655 cm^{-1}, 2,855 cm^{-1}, and 2,945 cm^{-1} (Fig. 5*B*). A separate PCA showed that the same component was identified across donors, as outlined in the loading plot depicted in *SI Appendix*, Fig. 3. Statistical analysis of the scores of individual donors revealed a significant separation of substrate-adherent macrophages between all tested materials using only two PCs (Fig. 5*C*). Scores of substrate-activated MDMs were projected onto the PCA previously calculated (Fig. 5*D*) with polarized MDMs to determine whether the lipid spectra of substrate-activated macrophages are comparable to those of polarized macrophages (Fig. 5 *E* and *F*). PCA projection visualized a proximity of M2c MDMs and Ti A MDMs, which is in accordance with the increased expression of MCP-1 of MDMs cultured on Ti A. Notably, titanium-activated MDMs were, in

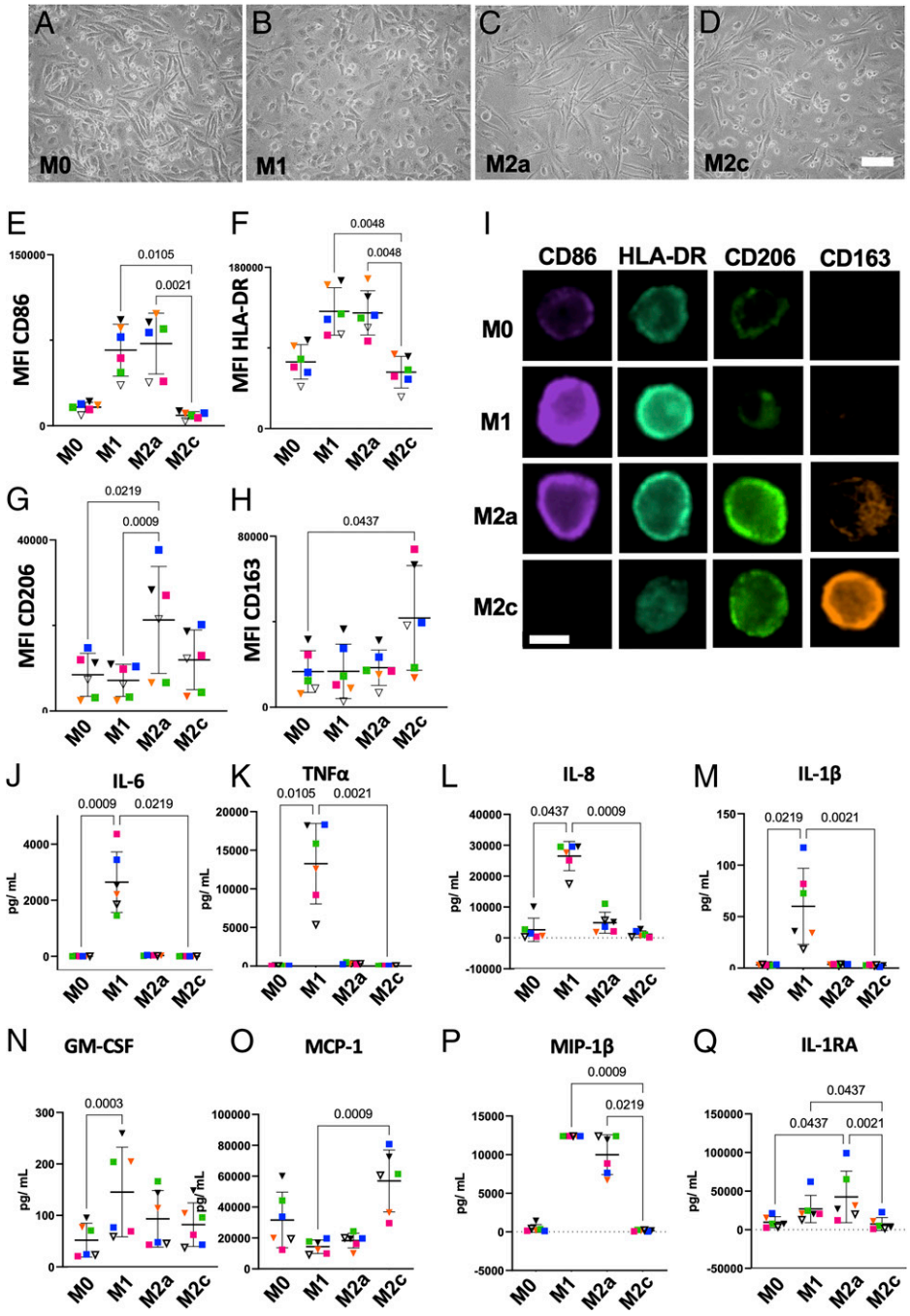

Fig. 1. Polarized MDMs display distinct morphological and physiological characteristics. (*A–D*) Brightfield images (10× magnification) show the morphology of polarized, human MDMs. (Scale bar, 50 μm.) (*E–H*) MFIs of polarization-associated surface antigens as measured by FC: CD86 (M1), HLA-DR (M1), CD206 (M2a), and CD163 (M2c). Data are presented as MFI ± SD. (*I*) ImageStream analyses provide representative immunofluorescence images of M0, M1, M2a, and M2c MDMs in suspension, stained for surface antigens CD86, HLA-DR, CD206, and CD163. (Scale bar, 20 μm.) (*J–Q*) Expression of common immunity-mediating cytokines measured by multiplex bead sandwich assay (Luminex). Data are presented as mean ± SD. Statistical significance was assessed using the Friedman test and Dunn's post hoc test ($n = 6$). Each donor has been assigned a unique color—male donors are indicated by squares and female donors by triangles.

general, more comparable with M2-polarized MDMs than with M1-polarized MDMs. In contrast, glass-activated macrophages were not comparable with the M1 or M2 MDMs.

Discussion

In this study, RM was utilized for a comprehensive characterization of stimulated MDMs to identify the MDM phenotypes M0, M1, M2a, and M2c and to determine MDM activation on titanium substrates. Our RM results suggest that the spectral information, especially the one containing the lipid component, can be a useful tool to monitor macrophage polarization and immune–metabolic processes both in suspension and material-adherent living cells.

Because macrophages are an extremely heterogenous cell population and many different culture systems exist to mature monocytes to macrophages, we placed special emphasis on a thorough characterization of the MDMs used in this work. Selection of culture plates, origin of supplemented serum (human, bovine, or other), and added stimulants such as LPS, interferons,

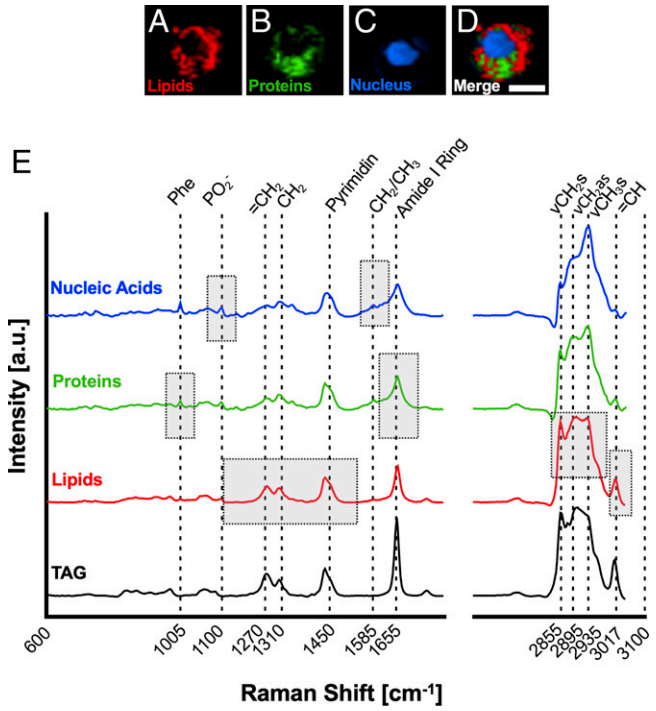

Fig. 2. Raman imaging resolves subcellular structures in MDMs. Identification of major cell component Raman signatures present in MDMs. (*A*–*D*) False color heat maps of (*A*) lipids (red), (*B*) proteins (green), (*C*) nucleic acids (blue), and (*D*) merged as identified by TCA. (Scale bar, 10 μm.) (*E*) Spectral fingerprints of MDM components. Boxes represent spectral areas typically associated with the biochemical fingerprint of the respective cell component. Phe = Phenylalanin, ν = stretching, s = symmetric, as = asymmetric. A typical, in house–measured TAG spectrum is shown for comparison.

or cytokines can significantly impact macrophage responses. In the cell-culture system for macrophage maturation, no significant up-regulation of proinflammatory cytokines such as TNF-α, IL-8, IL-6, or IL-1β was observed, indicating a robust resting level of M0 MDMs.

There are multiple studies using Raman spectra to distinguish between cell phenotypes or different stages of the cell cycle (25, 28, 29, 31); however, only few studies have investigated if RM can be employed to distinguish macrophage polarization. In 2018, Pavillon et al. described a machine-learning model for classification of binary macrophage activation based on morphological and biochemical information retrieved by quantitative phase imaging and analysis of Raman spectra (32). A study by Bertani et al. investigated binary macrophage activation, combining hyperspectral imaging, a method comparable to RM, and multivariate data analysis (33). Although these findings are in accordance with our results, as the most prominent separation also occurred between M0 and M1 MDMs, the Raman spectra in the previous studies were obtained from the complete cell as the ROI, but individual cellular substructures such as proteins, nucleic acids, or lipids were not resolved. In addition, the studies mentioned were limited to a binary classification of cell activation, separating resting and LPS-activated MDMs (32, 33). Here, we provide evidence that resolving cellular components can provide in-depth information regarding cell metabolism and immunity, enabling MDM classification into four distinct phenotypes. The most prominent differences appeared within the lipidome, separating groups of MDMs in the PCA scatter plot.

Macrophage activation, metabolism, and fatty acid composition are strongly related (34), which is reflected in the Raman spectra of lipids investigated in this study. In particular, Raman peaks that contributed to the separation of the different polarized groups were identified at 1,440 cm^{-1}, 1,655 cm^{-1}, 2,885 cm^{-1}, and 3,010 cm^{-1}—all peaks that are assigned to the C=C double bond of unsaturated fatty acids. Particularly of note is the olefinic stretch of C=C double bonds that are expressed at 1,655 cm^{-1} (24). A linear dependence of the C=C stretch at 1,655 cm^{-1} and the intensity of the CH_2 bending at 1,440 cm^{-1} has been previously reported and provides information about the overall content of unsaturated compared to saturated fatty acids in the cell (35). By comparing Raman spectra obtained in this study to spectra reported in the literature, we confirmed linoleic (36) and palmitoleic (37) acid as the main constituents of the macrophage lipids detected by RM (30). In addition, the peak at 1,744 cm^{-1} indicates the ester compound in TAGs (38). Lipids are known to regulate many cellular and immune functions such as energy storage or cell signaling. Polyunsaturated fatty acids like linoleic acid have profound effects on inflammatory processes by regulating expression of proinflammatory cytokines such as IL-1β or IL-6 (36). In this study, loading plots indicate that the degree of saturation in fatty acids substantially contributes to the separation of macrophage subtypes calculated by PCA. The capability of RM to trace lipids and lipid composition in macrophages has been previously shown (39–41), and lipids have been repeatedly reported to play important roles in inflammation and MDM polarization (34, 42, 43). In 2016, Montenegro-Burke et al. provided evidence that macrophage phenotypes significantly differ in their fatty acid composition (42). This is in accordance with other findings suggesting major metabolic shifts up to the Warburg effect in polarized macrophages (44), which extends (but is not limited to) protein function, cell signaling, or membrane composition. The metabolic shift that macrophages experience during the polarization process is intimately linked to changes in fatty acid composition and turnover, making lipid composition an ideal target to track macrophage polarization (34, 45, 46).

In this study, we aimed to assess if RM analysis can be utilized to monitor the lipidome of MDMs in vitro that have not been activated by classical stimuli like LPS or cytokines but by exposure to materials used for implants. PCA confirmed a significant separation within individual donors of glass and titanium but also between Ti M and Ti A, specimens that only differed in their surface topology. Based on the loading plots, this separation was again predominantly based on saturated versus unsaturated fatty acids and TAGs. Projection of substrate MDM data into the model of previously polarized MDMs further revealed that the means of M2c macrophages and Ti A macrophages were similar. This is in accordance with cytokine expression of MCP-1 and other studies that reported an anti-inflammatory, M2c-like phenotype on more textured topographies compared to smoother, oriented ones (18, 47, 48). Clinical research shows that implant roughness can lead to inflammation or fibrosis and therefore to poor clinical outcomes for patients that received dental and breast implants, linked to a prevalence of M2-like MDMs (49–51). As it had been previously shown, minor changes in cell physiology (e.g., due to exposure to surface roughness) are rarely comparable to activation of MDMs by LPS or IFN-γ (52). Our findings confirm this by showing that only few MDM polarization markers were increased on substrate-adherent MDMs when compared to M0 MDMs. However, macrophages are known to be sensitive to changes in stiffness, topography, or structure in their environment, and thus, these environmental factors play key roles in foreign body response and fibrosis, in which the environment is pathologically altered. Notably, the only significant increase of polarization indicators on titanium was detected in CD206, an M2a-associated scavenger receptor responsible for the uptake of bacterial sugars that is associated with fibrosis (53). In combination with an increase of MCP-1 on titanium substrates, these data hint at an M2a–M2c MDM phenotype on titanium

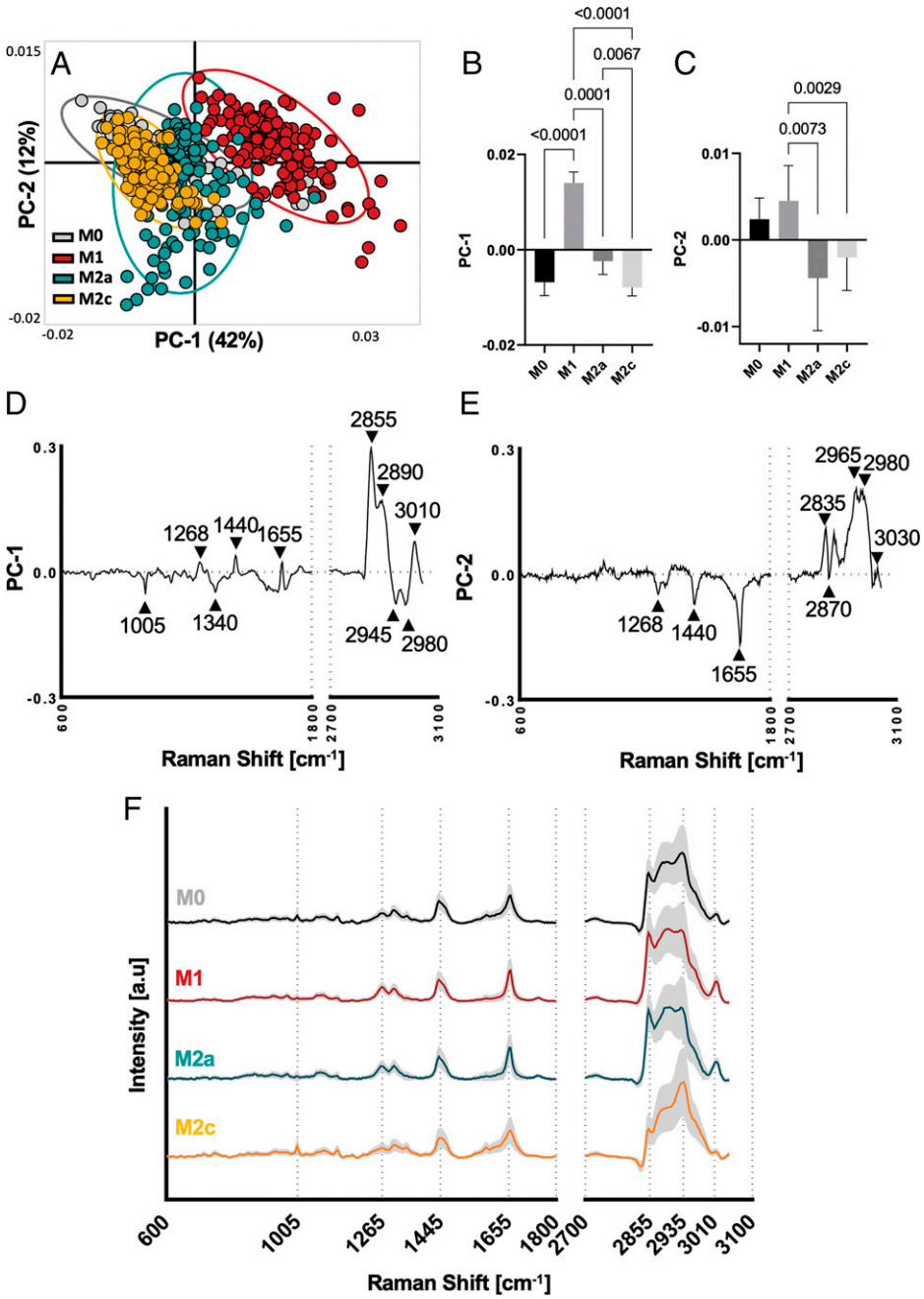

Fig. 3. PCA of Raman lipid spectra identifies significant differences between polarized MDMs. (*A*) Scatter plot of PC-1 (42%) and PC-2 (12%) visualizes spatial clustering of MDM polarization (confidence ellipse = 95%; each dot represents a single cell). (*B* and *C*) Statistical analyses of scores from PC-1 and PC-2 reveal significant differences between all four subtypes; one way ANOVA and Tukey's post hoc test, $n = 6$. (*D* and *E*) Loading plots describing major Raman peaks contribute to PCA separation. Peak assignments are listed in *SI Appendix*, Table 1. (*F*) Average lipid component Raman spectra of polarized MDMs with subtypes shown in black (M0), red (M1), blue (M2a), and yellow (M2c).

with a shift toward the M2c phenotype on the rougher titanium surface, which is confirmed by our RM data. This also corresponds to the results of previous studies, which reported an increase in anti-inflammatory phenotypes of MDMs cultured on rough surfaces in vitro (47, 48).

In summary, in this study, we demonstrated that Raman-based analytical methods combined with statistical analysis can noninvasively and marker-independently distinguish between different macrophage subtypes in situ. The lipidome of the cells was identified as a potent indicator for macrophage phenotype discrimination and for the analysis of adherent cells, which is especially helpful for the field of biomedical materials research.

Materials and Methods

All experiments using human samples in this study were approved by the ethics committee of the University Hospital of Tübingen (Institutional Review Board No. 495/2018BO2). Informed consent was obtained from all donors.

Material Preparation. Sterile Ti 15-mm disks with Ti M and Ti A surfaces were provided by the Institut Straumann AG. Disks were prepared and characterized as previously described (48, 54). Briefly, Ti M had a roughness of 0.1 μm and Ti A 0.3 μm. Contact angles of both materials were in the moderate hydrophilic range of about 62° to 77°. Glass coverslips were baked for 4 h at 200 °C for endotoxin removal and sterilization, then used immediately for cell-culture experiments.

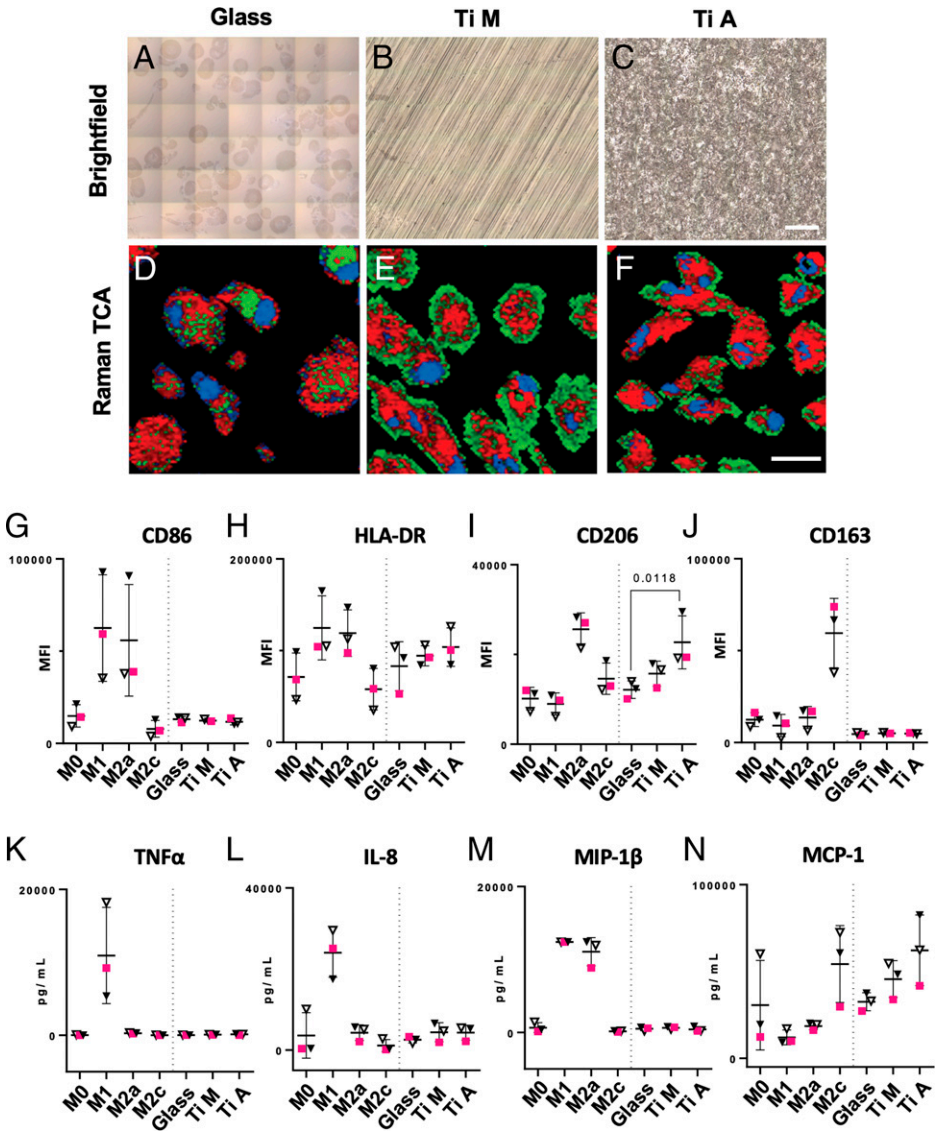

Fig. 4. RM allows real-time in situ analysis of MDMs on biomaterial surfaces. Raman analysis of MDMs cultured on biomaterial surfaces: (*A–C*) stitched brightfield images of glass, Ti M, and Ti A with MDMs adherent to the respective surface. (Scale bar, 100 μm.) (*D–F*) Spectral components of RM measurements identified by TCA with lipids color coded in red, proteins in green, and nuclei in blue. (Scale bar, 20 μm.) Images were acquired at 63× magnification. (*G–J*) MFIs of MDM surface markers analyzed by FC. MFIs of surface markers from MDMs cultured on biomaterials were plotted in the same graph as data obtained by polarization experiments (M0 through M2c). (*K–N*) Expression levels of four representative cytokines expressed by MDMs. The results were plotted in the same graph as data obtained by polarization experiments (M0 through M2c). Statistical analysis in graphs *G–N* was performed by Friedman's test and Dunn's post hoc test, and only results for substrate-adherent MDMs are shown. Data are shown as mean ± SD. Male donors are indicated by squares and female donors by triangles.

Monocyte Isolation and Culture. Whole blood was collected from healthy volunteers, and isolation procedures were performed immediately after collection. To separate peripheral blood mononuclear cells (PBMCs) from erythrocytes and granulocytes, density gradient centrifugation using SepMate tubes and Lymphoprep (both from Stemcell) was performed according to the manufacturer's instructions. In brief, fresh whole blood containing ethylendiamintetraacetate (EDTA) was diluted 1:1 with phosphate-buffered saline (PBS), layered over Lymphoprep in SepMate tubes, and separated by density gradient centrifugation. Supernatants containing PBMCs were decanted into fresh 50-mL falcon tubes and washed twice with PBS. PBMCs were then resuspended in cryopreservation medium (10% dimethyl sulfoxide, 20% fetal bovine serum [FBS], and 70% RPMI 1640 growth medium). For long-term storage, PBMCs were frozen at a concentration of 1×10^7cells/mL at −150 °C. Before seeding, cells were counted using a hemocytometer. Cell viability was assessed using trypan blue. Monocytes were isolated by plastic adherence from frozen PBMCs as described by Delirezh et al. (55). PBMCs were seeded at a concentration of 5×10^6 cells/cm^2 and allowed to adhere for 2 h at 37 °C and 5% CO_2 in culture medium. Nonadherent cells were then aspirated and removed. The remaining adherent monocytes were washed with PBS and continually cultured to mature into macrophages.

Macrophage Maturation and Polarization. Monocytes were cultured in RPMI 1640 containing Glutamax supplemented with 100 μg/mL streptomycin, 100 U/mL penicillin, and 10% heat-inactivated FBS (all from Thermo Fisher Scientific) at 37 °C and under a 5% CO_2 atmosphere in polystyrene 24-well cell-culture plates. Adherent monocytes were matured to macrophages over a period of 8 d in culture medium supplemented with 50 ng/mL macrophage colony-stimulating factor (Biolegend) at 37 C and 5% CO_2. Medium was changed at day 3. On day 5 of culture, medium was changed again, and stimulants were added to induce macrophage polarization: M1 (100 ng/mL LPS + 100 ng/mL IFN-γ), M2a (40 ng/mL IL-4 + 20 ng/mL IL-13), and M2c (20 ng/mL IL-10). LPS (*Escherichia coli*, O111:B4) was purchased from Merck Millipore. Protocols for macrophage polarization were adapted after Spiller et al. (56). IFN-γ and

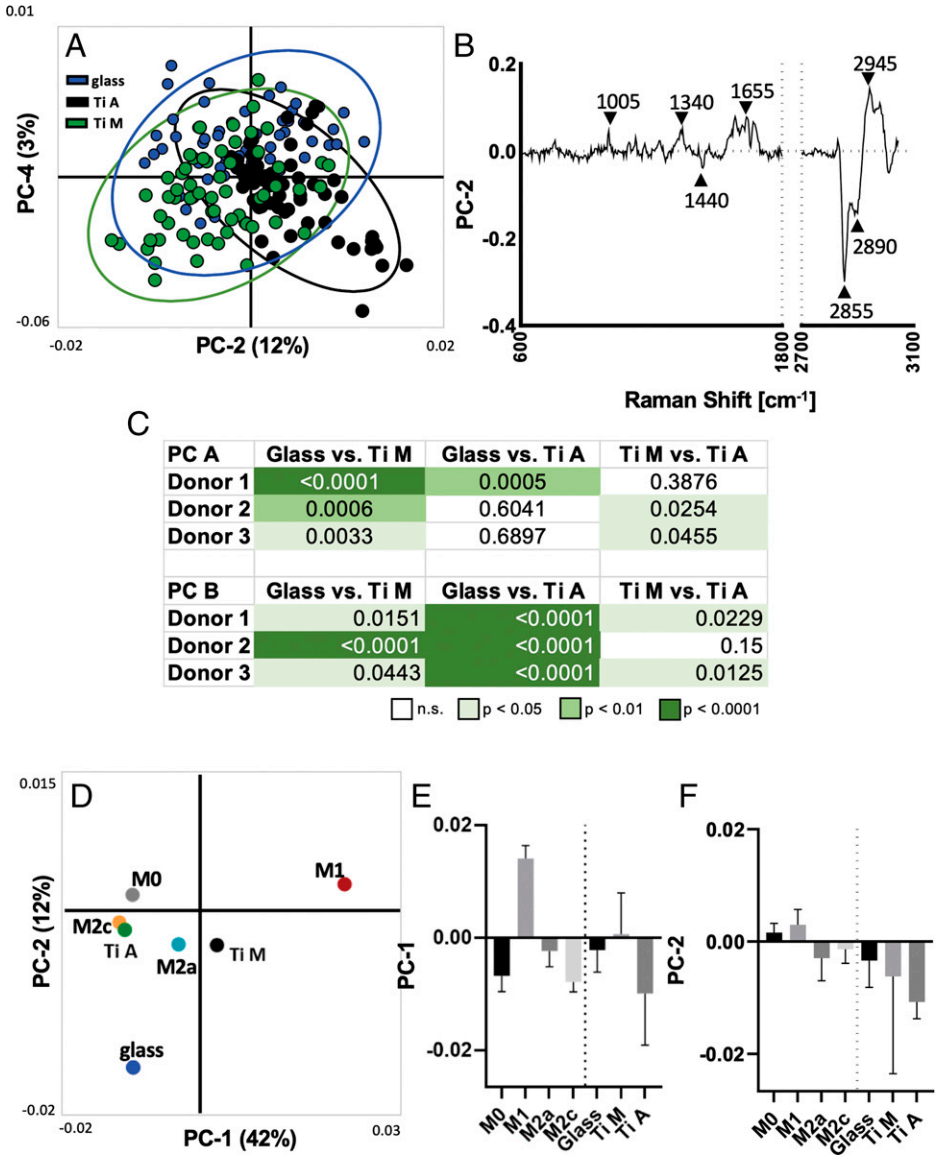

Fig. 5. RM lipid spectra can be used to distinguish substrate-adherent MDMs, and projected scores indicate proximity to polarization status. (*A*) Scatter plot of PC-2 (12%) and PC-4 (3%) visualizes spatial clustering of substrate-adherent MDMs (confidence ellipse = 95%; each dot represents a single cell). (*B*) Loading plot of PC-2 describes major Raman peaks contributing to PCA separation, comparable to those observed in polarized MDMs. (*C*) Statistical analysis of relevant components (PC A and PC B) reveal significant differences within single donors between substrates. (*D*) Projection of average substrate-adherent MDM scores into the PCA scores plot of the polarized MDMs. (*E* and *F*) Statistical comparison of mean score values ± SD. Only the projected scores were analyzed for significance using the Kruskal–Wallis and Dunn's post hoc tests.

cytokines were all purchased from Biolegend. M0 (resting) macrophages were not stimulated, but medium was changed on days 3 and 5. Likewise, monocytes cultured on biomaterials were not stimulated and were treated as M0.

FC. Before dissociation, cells were washed three times with fluorescence-activated cell sorting (FACS) buffer (PBS + 2% FBS + 0.05 Mm NaN_3 + 0.1 Mm EDTA) to deplete cells of bivalent cations. Adherent macrophages were then detached by incubation with Accutase (Biolegend) for 10 min at 37 °C and 5% CO_2. For FC analysis, harvested cells were blocked with 10% sterile-filtered, human, male AB serum (H2B) in FACS buffer for 20 min at 4 °C to prevent nonspecific binding of antibodies. For cell-surface marker staining, the following antibodies were used: CD86-Pacific Blue (clone IT2.2), HLA-DR-Brilliant Violet 510 (clone L243), CD206-FITC (fluorescein isothiocyanate) (clone 15-2), and CD163-PE/Cy7 (clone RM3/1) (Biolegend). For staining, all antibodies were diluted 1:50 with FACS buffer, and cells were stained for 30 min at 4 °C in the dark and washed with FACS buffer subsequently. Data were acquired using a BD Biosciences LSRFortessa Cytometer and analyzed using FlowJo 10.4.2 (Tree Star). Cells were gated using forward scatter versus sideward scatter properties to exclude debris, doublets, and dead cells (7-AAD staining, Biolegend). MFIs of the whole macrophage population were analyzed. Compensation controls were run for each experiment using software-based automatic compensation to consider potential fluorescence spillover. In addition, fluorescence minus one controls were run to determine performance of the antibody panel and the fluorescence-staining pattern of each individual antibody.

Imaging FC. Macrophages were detached, processed, and stained as described for regular FC analysis. Dead cells were excluded using the Zombie NIR fixable viability kit (Biolegend). At least 1×10^4 cells per sample were acquired by the ImageStreamX mkII (Luminex Corporation) with the INSPIRE instrument controller software with 40× magnification. Data were analyzed with IDEAS image analysis software. All samples were gated on single cells in focus that were Zombie NIR negative. An unstained control sample was used to determine background fluorescence.

Cytokine Analysis by Multiplexed Bead-Based Sandwich Immunoassay. Cell-culture supernatants were collected on day 8, centrifuged at 5,000 rpm for 3 min, and stored at −80 °C until analysis. Levels of IL-6, IL-8, TNF-α, IL-1β, IL-1RA, MCP-1, MIP-1β, and granulocyte-macrophage colony-stimulating

factor (GM-CSF) were determined using a set of "in house–developed" Luminex-based sandwich immunoassays each consisting of commercially available capture and detection antibodies and calibrator proteins. All assays were thoroughly validated ahead of the study with respect to accuracy, precision, parallelism, robustness, specificity, and sensitivity (57). Samples were diluted at least 1:2 or higher. After incubation of the prediluted samples or calibrator protein with the capture-coated microspheres, beads were washed and incubated with biotinylated detection antibodies. Streptavidin–phycoerythrin was added after an additional washing step for visualization. For control purposes, calibrators and quality control samples were included on each microtiter plate. All measurements were performed on a Luminex FlexMap 3D analyzer system, using Luminex xPONENT 4.2 software (Luminex). For data analysis, MasterPlex QT version 5.0 was employed. Standard curve and quality control samples were evaluated according to internal criteria adapted to the Westgard Rules [3] to ensure proper assay performance.

RM. RM analysis of macrophages was performed on a customized WITec Raman system (WITec GmbH) equipped with a green laser (532 nm) and a charge-coupled device spectrograph with a grating of 600 g/mm. Images were acquired using a 63× apochromat water-immersion objective, an integration time of 0.5 s, a pixel resolution of 1×1 μm, and a laser power of 50 mW for cells in suspension or 25 mW for adherent cells. Macrophages adherent to glass or titanium disks were stained with FITC–phalloidin before analysis to locate cells and ROIs. All cells were fixed with 4% paraformaldehyde for 10 min at room temperature before Raman analysis. For each donor and subtype, 30 cells were measured.

Data Processing. Raman data were processed using the Project FIVE 5.2 software (WITec GmbH). Cosmic rays were removed, and a baseline correction was employed on all spectra. All preprocessing steps were published previously in detail (58). Spectra were cropped from the range of 300 cm^{-1} to 3,045 cm^{-1}. TCA was employed to identify nucleic acids, proteins, and lipids. In brief, TCA is a nonnegative matrix factorization-based multivariate analysis tool that identifies dominant spectral components in a dataset. These components can then be visualized by false color intensity distribution heat maps. To extract single spectra for each of the three cellular components, masks were generated based on TCA heat maps. A total of 2% of the most intense spectra were extracted, and a total average spectrum per cell was calculated. To reduce dimensionality of the spectral data, PCA was performed using the Unscrambler X 14.0 software (Camo Software). PCA is an exploratory, linear transformation technique used to increase interpretability of the data while minimizing information loss. It accomplishes dimensionality reduction by calculating eigenvectors of the data's covariance matrix (58, 59). Here, spectral ranges of 400 to 1,800 cm^{-1} and 2,700 to 3,045 cm^{-1} were investigated by PCA analysis. PCA results are presented as score plots and loading plots. The 95% confidence ellipses were calculated using Origin Pro-9.1 software (OriginLab). Loadings show the original variables' contribution to the component and were used to identify relevant and comparable PCs for further analysis.

Statistical Analysis. All relevant statistical parameters such as sample size, replicate types, and *P* values are described in the corresponding figures. Donors are represented by *n*. For polarized macrophages, six donors were analyzed, and for substrate macrophages, three donors were analyzed. Gaussian distributions of data were tested using the Kolmogorov–Smirnov test. Unless otherwise indicated, data were analyzed for significance using the Kruskal–Wallis test with Dunn's post hoc test with Graph Pad Prism 8.0.0 (Graph Pad Software, Inc.). *P* values <0.05 were considered significant.

Data Availability. All study data are included in the article and/or *SI Appendix*.

ACKNOWLEDGMENTS. We thank Simone Pöschel (ImageStream Core Facility, University Hospital Tübingen) for her assistance with the ImageStream measurements. We also express our gratitude to Svenja Hinderer, Elena Rapp, and Bernadette Walter (Natural and Medical Sciences Institute Reutlingen), as well as Simone Liebscher (University of Tübingen), for their excellent technical support and scientific discussions. We thank Shannon Lee Layland (University of Tübingen) for his helpful comments on the manuscript. This work was financially supported by the Ministry of Baden-Württemberg for Economic Affairs, Labor, and Tourism; the Ministry of Science, Research, and the Arts of Baden-Württemberg (Grant SI-BW 01222-91 to K.S.-L.); and the Deutsche Forschungsgemeinschaft (Grants INST 2388/33-1, INST 2388/64-1, GRK 2543/1, and Germany's Excellence Strategy EXC 2180-390900677 all to K.S.-L.).

1. S. A. Eming, T. A. Wynn, P. Martin, Inflammation and metabolism in tissue repair and regeneration. *Science* **356**, 1026–1030 (2017).
2. C. J. Ferrante, S. J. Leibovich, Regulation of macrophage polarization and wound healing. *Adv. Wound Care (New Rochelle)* **1**, 10–16 (2012).
3. M. Lech, H.-J. Anders, Macrophages and fibrosis: How resident and infiltrating mononuclear phagocytes orchestrate all phases of tissue injury and repair. *Biochim. Biophys. Acta* **1832**, 989–997 (2013).
4. J. W. Godwin, N. Rosenthal, Scar-free wound healing and regeneration in amphibians: Immunological influences on regenerative success. *Differentiation* **87**, 66–75 (2014).
5. J. W. Godwin, A. R. Pinto, N. A. Rosenthal, Macrophages are required for adult salamander limb regeneration. *Proc. Natl. Acad. Sci. U.S.A.* **110**, 9415–9420 (2013).
6. K. Y. Gerrick *et al.*, Transcriptional profiling identifies novel regulators of macrophage polarization. *PLoS One* **13**, e0208602 (2018).
7. Y. Okabe, R. Medzhitov, Tissue-specific signals control reversible program of localization and functional polarization of macrophages. *Cell* **157**, 832–844 (2014).
8. Y.-C. Liu, X.-B. Zou, Y.-F. Chai, Y.-M. Yao, Macrophage polarization in inflammatory diseases. *Int. J. Biol. Sci.* **10**, 520–529 (2014).
9. P. J. Murray *et al.*, Macrophage activation and polarization: Nomenclature and experimental guidelines. *Immunity* **41**, 14–20 (2014).
10. D. M. Mosser, J. P. Edwards, Exploring the full spectrum of macrophage activation. *Nat. Rev. Immunol.* **8**, 958–969 (2008).
11. L. Chung, D. R. Maestas Jr., F. Housseau, J. H. Elisseeff, Key players in the immune response to biomaterial scaffolds for regenerative medicine. *Adv. Drug Deliv. Rev.* **114**, 184–192 (2017).
12. J. M. Anderson, K. M. Miller, Biomaterial biocompatibility and the macrophage. *Biomaterials* **5**, 5–10 (1984).
13. N. J. Hallab, Biologic responses to orthopedic implants: Innate and adaptive immune responses to implant debris. *Spine* **41**, S30–S31 (2016).
14. J. M. Anderson, S. Jiang, "Implications of the acute and chronic inflammatory response and the foreign body reaction to the immune response of implanted biomaterials" in *The Immune Response to Implanted Materials and Devices*, B. Corradetti, Ed. (Springer, 2017), pp. 15–36.
15. J. L. Dziki *et al.*, Solubilized extracellular matrix bioscaffolds derived from diverse source tissues differentially influence macrophage phenotype. *J. Biomed. Mater. Res. A* **105**, 138–147 (2017).
16. D. Abebayehu *et al.*, Galectin-1 promotes an M2 macrophage response to polydioxanone scaffolds. *J. Biomed. Mater. Res. A* **105**, 2562–2571 (2017).
17. N. Araújo-Gomes *et al.*, Complement proteins regulating macrophage polarisation on biomaterials. *Colloids Surf. B Biointerfaces* **181**, 125–133 (2019).
18. K. A. Barth, J. D. Waterfield, D. M. Brunette, The effect of surface roughness on RAW 264.7 macrophage phenotype. *J. Biomed. Mater. Res. A* **101**, 2679–2688 (2013).
19. M. Bartneck *et al.*, Inducing healing-like human primary macrophage phenotypes by 3D hydrogel coated nanofibres. *Biomaterials* **33**, 4136–4146 (2012).
20. V. Bonito *et al.*, Modulation of macrophage phenotype and protein secretion via heparin-IL-4 functionalized supramolecular elastomers. *Acta Biomater.* **71**, 247–260 (2018).
21. M. Waters, P. VandeVord, M. Van Dyke, Keratin biomaterials augment anti-inflammatory macrophage phenotype in vitro. *Acta Biomater.* **66**, 213–223 (2018).
22. Z. Ye, C. A. Sarkar, Towards a quantitative understanding of cell identity. *Trends Cell Biol.* **28**, 1030–1048 (2018).
23. R. Smith, K. L. Wright, L. Ashton, Raman spectroscopy: An evolving technique for live cell studies. *Analyst (Lond.)* **141**, 3590–3600 (2016).
24. J. R. Beattie, S. E. J. Bell, B. W. Moss, A critical evaluation of Raman spectroscopy for the analysis of lipids: Fatty acid methyl esters. *Lipids* **39**, 407–419 (2004).
25. R. Daum, E. M. Brauchle, D. A. C. Berrio, T. P. Jurkowski, K. Schenke-Layland, Non-invasive detection of DNA methylation states in carcinoma and pluripotent stem cells using Raman microspectroscopy and imaging. *Sci. Rep.* **9**, 7014 (2019).
26. N. Stone, C. Kendall, J. Smith, P. Crow, H. Barr, Raman spectroscopy for identification of epithelial cancers. *Faraday Discuss.* **126**, 141–157 (2004).
27. J. M. Surmacki, B. J. Woodhams, A. Haslehurst, B. A. J. Ponder, S. E. Bohndiek, Raman micro-spectroscopy for accurate identification of primary human bronchial epithelial cells. *Sci. Rep.* **8**, 12604 (2018).
28. E. Brauchle, S. Thude, S. Y. Brucker, K. Schenke-Layland, Cell death stages in single apoptotic and necrotic cells monitored by Raman microspectroscopy. *Sci. Rep.* **4**, 4698 (2014).
29. J. Marzi, E. M. Brauchle, K. Schenke-Layland, M. W. Rolle, Non-invasive functional molecular phenotyping of human smooth muscle cells utilized in cardiovascular tissue engineering. *Acta Biomater.* **89**, 193–205 (2019).
30. K. Czamara *et al.*, Raman spectroscopy of lipids: A review. *J. Raman Spectrosc.* **46**, 4–20 (2015).
31. M. Pudlas, E. Brauchle, T. J. Klein, D. W. Hutmacher, K. Schenke-Layland, Non-invasive identification of proteoglycans and chondrocyte differentiation state by Raman microspectroscopy. *J. Biophotonics* **6**, 205–211 (2013).
32. N. Pavillon, A. J. Hobro, S. Akira, N. I. Smith, Noninvasive detection of macrophage activation with single-cell resolution through machine learning. *Proc. Natl. Acad. Sci. U.S.A.* **115**, E2676–E2685 (2018).
33. F. R. Bertani *et al.*, Classification of M1/M2-polarized human macrophages by label-free hyperspectral reflectance confocal microscopy and multivariate analysis. *Sci. Rep.* **7**, 8965 (2017).

34. A. Batista-Gonzalez, R. Vidal, A. Criollo, L. J. Carreño, New insights on the role of lipid metabolism in the metabolic reprogramming of macrophages. *Front. Immunol.* **10**, 2993 (2020).
35. H. Wu *et al.*, In vivo lipidomics using single-cell Raman spectroscopy. *Proc. Natl. Acad. Sci. U.S.A.* **108**, 3809–3814 (2011).
36. S. D. Pauls *et al.*, Anti-inflammatory effects of α-linolenic acid in M1-like macrophages are associated with enhanced production of oxylipins from α-linolenic and linoleic acid. *J. Nutr. Biochem.* **57**, 121–129 (2018).
37. S. Wang *et al.*, In vitro fatty acid enrichment of macrophages alters inflammatory response and net cholesterol accumulation. *Br. J. Nutr.* **102**, 497–501 (2009).
38. H. Takahashi, A. Yanamisawa, S. Kajimoto, T. Nakabayashi, Observation of the changes in the chemical composition of lipid droplets using Raman microscopy. *Phys. Chem. Chem. Phys.* **22**, 21646–21650 (2020).
39. C. Matthäus *et al.*, "Monitoring intra-cellular lipid metabolism in macrophages by Raman-and CARS-microscopy" in *Biophotonics: Photonic Solutions for Better Health Care II*, J. Popp, W. Drexler, V. V. Tuchin, D. L. Matthews, Eds. (SPIE, 2010), pp. 771511.
40. C. Matthäus *et al.*, Noninvasive imaging of intracellular lipid metabolism in macrophages by Raman microscopy in combination with stable isotopic labeling. *Anal. Chem.* **84**, 8549–8556 (2012).
41. C. Stiebing *et al.*, Raman imaging of macrophages incubated with triglyceride-enriched oxLDL visualizes translocation of lipids between endocytic vesicles and lipid droplets. *J. Lipid Res.* **58**, 876–883 (2017).
42. J. R. Montenegro-Burke *et al.*, Lipid profiling of polarized human monocyte-derived macrophages. *Prostaglandins Other Lipid Mediat.* **127**, 1–8 (2016).
43. V. Bhaskar *et al.*, Monoclonal antibodies targeting IL-1 beta reduce biomarkers of atherosclerosis in vitro and inhibit atherosclerotic plaque formation in apolipoprotein E-deficient mice. *Atherosclerosis* **216**, 313–320 (2011).
44. E. M. Palsson-McDermott *et al.*, Pyruvate kinase M2 regulates Hif-1α activity and IL-1β induction and is a critical determinant of the Warburg effect in LPS-activated macrophages. *Cell Metab.* **21**, 65–80 (2015).
45. J. Korbecki, K. Bajdak-Rusinek, The effect of palmitic acid on inflammatory response in macrophages: An overview of molecular mechanisms. *Inflamm. Res.* **68**, 915–932 (2019).
46. S.-S. Im *et al.*, Linking lipid metabolism to the innate immune response in macrophages through sterol regulatory element binding protein-1a. *Cell Metab.* **13**, 540–549 (2011).
47. Y. Zhang, X. Cheng, J. A. Jansen, F. Yang, J. J. J. P. van den Beucken, Titanium surfaces characteristics modulate macrophage polarization. *Mater. Sci. Eng. C* **95**, 143–151 (2019).
48. K. M. Hotchkiss *et al.*, Titanium surface characteristics, including topography and wettability, alter macrophage activation. *Acta Biomater.* **31**, 425–434 (2016).
49. F. Jordana, L. Susbielles, J. Colat-Parros, Periimplantitis and implant body roughness: A systematic review of literature. *Implant Dent.* **27**, 672–681 (2018).
50. D. J. Cohen *et al.*, Performance of laser sintered Ti-6Al-4V implants with bone-inspired porosity and micro/nanoscale surface roughness in the rabbit femur. *Biomed. Mater.* **12**, 025021 (2017).
51. M. Atlan, G. Nuti, H. Wang, S. Decker, T. Perry, Breast implant surface texture impacts host tissue response. *J. Mech. Behav. Biomed. Mater.* **88**, 377–385 (2018).
52. N. Bloise *et al.*, Engineering immunomodulatory biomaterials for regenerating the infarcted myocardium. *Front. Bioeng. Biotechnol.* **8**, 292 (2020).
53. J. Wang *et al.*, Microcystin-LR ameliorates pulmonary fibrosis via modulating $CD206^+$ M2-like macrophage polarization. *Cell Death Dis.* **11**, 136 (2020).
54. G. Zhao *et al.*, High surface energy enhances cell response to titanium substrate microstructure. *J. Biomed. Mater. Res. A* **74**, 49–58 (2005).
55. N. Delirezh, E. Shojaeefar, P. Parvin, B. Asadi, Comparison the effects of two monocyte isolation methods, plastic adherence and magnetic activated cell sorting methods, on phagocytic activity of generated dendritic cells. *Cell J.* **15**, 218–223 (2013).
56. K. L. Spiller *et al.*, The role of macrophage phenotype in vascularization of tissue engineering scaffolds. *Biomaterials* **35**, 4477–4488 (2014).
57. J. O. Westgard, P. L. Barry, M. R. Hunt, T. Groth, A multi-rule Shewhart chart for quality control in clinical chemistry. *Clin. Chem.* **27**, 493–501 (1981).
58. A. Zbinden *et al.*, Non-invasive marker-independent high content analysis of a microphysiological human pancreas-on-a-chip model. *Matrix Biol.* **85-86**, 205–220 (2020).
59. I. T. Jolliffe, J. Cadima, Principal component analysis: A review and recent developments. *Philos. Trans.- Royal Soc., Math. Phys. Eng. Sci.* **374**, 20150202 (2016).